Available online at www.sciencedirect.com
SCIENCE DIRECT®
International Journal of Rock Mechanics & Mining Sciences 41 (2004) 1427–1445
International Journal of Rock Mechanics and Mining Sciences
www.elsevier.com/locate/ijrmms

Innovative laboratory testing

J.S.O. Lau[a,*], N.A. Chandler[b]

[a]JSO Lau Consulting Services Inc., 12 Country Club Drive, Ottawa, Ontario, Canada K1V 9W2
[b]Atomic Energy of Canada Limited, Pinawa, Manitoba, Canada R0E 1L0

Accepted 9 September 2004

Abstract

Three laboratory test techniques were developed to study and quantify damage development in loaded rock specimens and to provide data for use in the calibration and solution of numerical models. Damage-controlled tests involved incremental loading–unloading cycles with the stress at volumetric strain reversal (crack damage stress σ_{cd}) and elastic properties calculated for each successive cycle. Damage was quantified by measuring the irreversible volumetric strain upon unloading and the degradation of rock strength and elastic properties. In long-term loading tests, a creep stress greater than σ_{cd} was applied to the specimen until failure. The time to failure was dependent upon the ratio of the creep stress to σ_{cd}, and to confining pressure. It was shown that σ_{cd} is a reasonable estimate of the long-term rock strength. Damage was quantified by measuring the degradation of elastic properties through periodic unloading–reloading cycles. The test data were used for the calibration of Itasca's PFC stress-corrosion model. Five types of thermoporoelasticity tests were designed to determine seven of the nine thermoporoelastic parameters required for the modelling of the thermoporoelastic response of rock. Tests were performed by applying increments of confining pressure, temperature or pore pressure on the rock specimen, and measuring the changes in confining pressure, specimen volume and pore pressure. The measured values of five parameters were found to agree reasonably well with the estimated values.

1. Introduction

In the design of a deep geologic repository, it is important not only to know the long-term in situ strength of rocks, but also to minimize potential pathways for the transport of water-borne radionuclides in rocks surrounding the repository. Potential pathways could be created if the rock around an excavation is damaged due to stress redistribution. This damage appears in the form of cracking in the rock. In addition, increased water pressure in the pores and microcracks of the rock due to heating could cause tensile fracturing resulting in increased hydraulic conductivity and could alter the existing hydraulic gradients, potentially affecting the transport of radionuclides as a result of changes in both the quantity of flow through the rock and the flow direction. Repository designers will therefore need to understand the micro-mechanisms involved in the process leading to the creation and growth of cracks and to quantify the expected damage to the rocks around excavations over the very long lifetime of the repository.

Atomic Energy of Canada Limited (AECL) and Ontario Power Generation Incorporated (OPG) have conducted a comprehensive study to develop an integrated modelling, characterization and monitoring system required to design and monitor the excavation for a nuclear fuel waste repository [1–4]. This work is focused at AECL's Underground Research Laboratory (URL) near Lac du Bonnet, Manitoba. Many advances in rock mechanics were made during the implementation and analyses of large-scale in situ experiments conducted at the URL [5–7]. Excavation stability analyses showed that the crack damage stress of rock corresponding to volumetric strain reversal, determined in laboratory tests, was indicative of the long-term strength of the rock [8]. New approaches to discrete element

*Corresponding author. Tel.: +1 613 738 3825; fax: +1 613 739 1027.
E-mail address: joseph097@sympatica.ca (J.S.O. Lau).

1365-1609/$ - see front matter © 2004 Elsevier Ltd. All rights reserved.
doi:10.1016/j.ijrmms.2004.09.008

modelling of rock behaviour showed that the time-dependent Particle Flow Code (PFC) [9] stress-corrosion model, calibrated to laboratory test data, can provide a good simulation of the excavation response of rock [10–12]. Back-analysis of the thermally induced pore pressure field demonstrated that the pore pressure could be modelled using the theory of thermoporoelasticity [13], requiring several thermoporoelastic parameters to be measured in the laboratory.

Laboratory testing was an important component of the study at the URL. Many standard and non-standard tests were carried out in support of the URL rock mechanics program [14–16]. Traditional tests included uniaxial and triaxial compression, post-failure, and tensile tests. Non-traditional tests were developed: (1) to provide a measure of in situ long-term rock strength, or degradation of rock strength as a function of time; (2) to provide data for use in quantifying the evolution of rock damage as a function of the magnitude and duration of the applied stresses; (3) to provide data for use in calibration of numerical models for excavation stability analysis; and (4) to determine the parameters for use in solutions for thermoporoelasticity for the modelling of rock pore pressure. Non-traditional tests included damage-controlled tests, long-term loading tests and thermoporoelasticity tests, which are the subjects of this paper. These tests were developed and conducted at the Mining and Mineral Sciences Laboratories (MMSL) operated by Natural Resources Canada in Ottawa, Ontario. This paper provides a brief overview of the damage evolution in rock and thermoporoelasticity parameters, describes the damage-controlled, long-term loading and thermoporoelasticity tests, presents representative data and discusses relevant findings and experimental techniques.

2. Damage evolution in rock

Many researchers have investigated failure processes in brittle rock [17–22]. These researchers showed that the stress-strain curves for a brittle material under compression could be divided into four phases: (I) crack closure, (II) linear elasticity, (III) stable crack growth and (IV) unstable crack growth (Fig. 1). The crack initiation stress, σ_{ci}, is defined as the stress level marking the onset of dilation and the beginning of Phase III where the plot of stress versus strain deviates from linear elastic behaviour, indicating the development and growth of stable cracks. These cracks are referred to as stable cracks since an increase in load is required to cause further cracking, and time-dependent crack growth does not occur under constant load. The crack damage stress, σ_{cd}, is defined by Martin [23] as the stress level marking the beginning of Phase IV where the volumetric strain reversal occurs, indicating that the

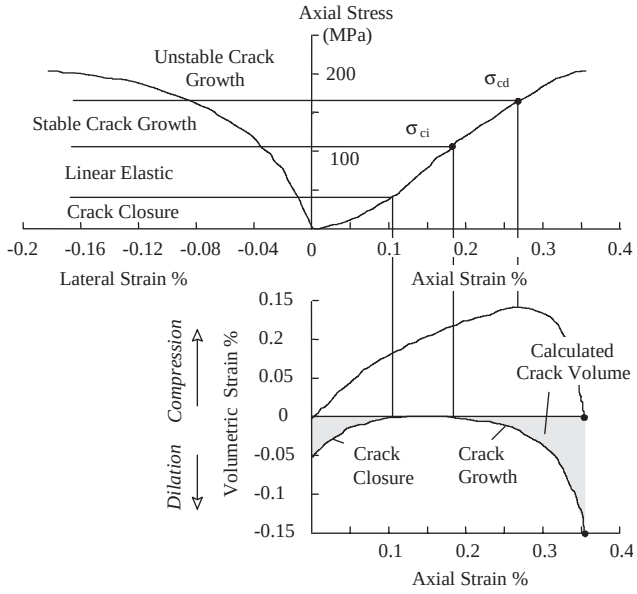

Fig. 1. Typical stress versus strain relationships for a brittle rock.

dilation due to the formation and growth of cracks exceeds the elastic compression of the rock resulting from increased load. Loading a sample above σ_{cd} results in time-dependent increases in damage to the material, leading to ultimate sample failure under a sustained constant load. The crack damage stress, therefore, is believed to be indicative of the long-term strength of the rock [22].

During compression tests on brittle rocks, unconfined samples fail by axial splitting, whereas confined samples fail along shear planes. However, a closer investigation of the shear planes revealed a coalescence of smaller axially aligned microcracks [22], as illustrated in Fig. 2. The initiation and propagation of the axially aligned cracks, i.e., perpendicular to the least compressive stress direction, implies that internal microscopic tensions are developing within the rock sample in response to the macroscopic compression. Laboratory experiments reveal that brittle rocks exhibit a highly nonlinear and complex response under applied compressive stress. Microcracking processes due to local stress concentrations around micro-defects (such as pores, grain boundaries, inclusions and pre-existing cracks) are believed to be responsible for this complex behaviour. The micro-mechanisms involved include sliding along pre-existing microcracks, pore crushing and elastic mismatch between mineral grains [21]. In theory, frictional sliding on pre-existing cracks will result in the opening and propagation of tensile cracks (wing cracks) from the tips of the sliding crack [24]. Frictional sliding tends to result in shear strain, whereas the opening and propagation of wing cracks results in dilatency or increased volumetric strain and degradation

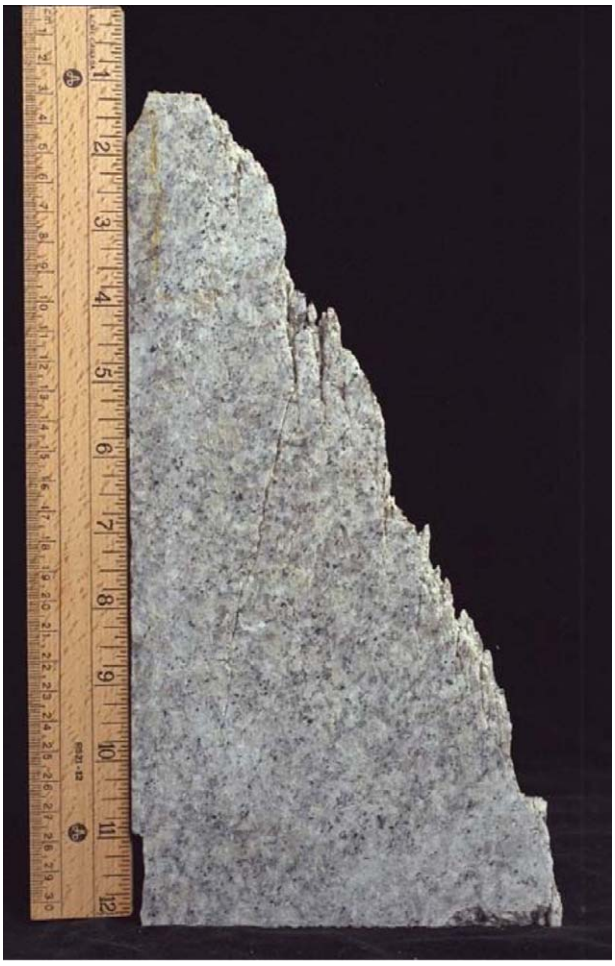

Fig. 2. Photograph of a failed sample, illustrating both axial cracking and macroscopic shear plane.

of material stiffness. The evolution of damage can therefore be represented as irreversible strain in rock samples with the permanent volumetric strain, indicative of the dilation due to cracking, being an important damage indicator.

In situ, stress redistribution around excavations can lead to compressive loading near the excavation surface above σ_{cd} as defined by unconfined laboratory tests. A progressive failure process is initiated that results in formation of notch-shaped breakout of rock in the high compressive stress regions around the excavation [22]. The progressive failure stabilizes as confinement increases at the apex of the notch. Numerical models developed to replicate this process must consider the increase in long-term strength with increasing confinement, the decrease in strength with increasing damage, changes in elastic properties with increasing damage, and the evolution of damage with respect to time under constant load. The damage-controlled tests and the long-term load tests, described in later sections of this paper, were conducted at the MMSL to provide data for calibration of numerical models developed to simulate the progressive failure processes observed at the URL [10,24].

3. Thermoporoelastic parameters

The integrity of the rock mass around a deep geologic repository is an important design issue. Temperature, pore water pressure and stress in the rock will evolve with time as a result of heat from the decay of radionuclides in the spent fuel. Temperature increase in low permeability rock will result in thermal expansion of the rock leading to an elastic decrease in pore volume. This process, coupled with the thermal-expansion of the water in the pores causes increases in pore pressure. The increase in pore pressure tends to reduce the compressive stress in the rock, introducing the possibility of tensile stress and hydraulic fracture [25]. The decrease in compressive stress is dependent upon the rate of increase in temperature relative to the rate of dissipation of pore pressure. Analysis of this phenomenon, therefore, requires a fully coupled thermo-hydro-mechanical model, making use of coupling parameters that are representative of the in situ material.

Coupled thermo-hydro-mechanical processes in rock mechanics can be analysed within the framework of the linear theory of thermoporoelasticity. Detournay et al. [26] combined constitutive equations with balanced laws (momentum, mass and energy) and conduction laws (Darcy and Fourier) to yield field equations for the displacement and changes in pore pressure and temperature with time. The various material constants (thermoporoelastic parameters), which appear in those field equations, can be organized into five groups of material properties:

(1) mechanical—shear modulus, G; drained bulk modulus, K
(2) thermal—drained thermal expansivity, β_d; volumetric heat capacity, C; thermal conductivity, κ^*
(3) hydromechanical—Biot coefficient, α; Biot modulus, M; Skempton coefficient, B; undrained bulk modulus, K_u
(4) thermo-hydro-mechanical—undrained thermal expansion coefficient, β_u; hydro-thermal coupling coefficient, β_m
(5) transport—hydraulic mobility coefficient, κ

Not all of these thermoporoelastic parameters are independent. Detournay and Berchenko [26] showed that only nine independent parameters are required to characterize the thermoporoelastic response of an isotropic rock.

A comprehensive suite of laboratory and field thermoporoelastic tests was conducted as part of the

Underground Research Laboratory experimental program [2]. These tests were designed to determine many of the above noted material parameters for Lac du Bonnet granite. Specialized thermoporoelastic laboratory tests were designed to directly measure the drained bulk modulus K, the drained and undrained expansivities, β_d and β_u, the hydromechanical coefficients B and K_u, and by determining the stiffness of the solid constituents K_s, the Biot coefficient α could be calculated. The hydro-thermal coefficient, β_m, was also determined by combining the results from the five different types of tests. The tests performed and their results are described later in this paper.

4. Rock type and specimen preparation

The rock type used in these non-traditional tests was Lac du Bonnet Batholith granite from the URL and from the nearby Cold Spring quarry. The 61-mm-diameter core samples were cut and prepared at the MMSL, with length-to-diameter ratios of approximately 2.5. The end surfaces of each specimen were ground flat to within 0.025 mm, parallel to each other to within 0.025 mm and perpendicular to the longitudinal axis of the specimen to within 0.25°.

Tests were performed on both air-dried and saturated specimens. Air-dried specimens were used for damage-controlled tests, however only the results from long-term load and thermoporoelastic tests using saturated specimens are reported here. A multi-cycle immersion/evacuation process [14] was used to saturate specimens. The water-saturated specimens were stored in distilled water until required for testing. The application of resistance strain gauges on specimens involved bonding one pair of axial gauges and one pair of circumferential gauges at mid-height of the specimen. Each pair consisted of diametrically opposed gauges connected in series to form a single active gauge. The gauge installation procedure is described in a later section.

5. Test equipment

The test machine was a computer-controlled, servo-hydraulic compression machine (MTS 815 Rock Mechanics Test System), consisting of a 2.2 MN rated load cell, load frame, test controller, triaxial cell, pressure intensifier assembly, TestStar II control system and microcomputer. The triaxial cell (Fig. 3) was equipped with a heater, heat shroud, thermocouples (located at the specimen top, midpoint and bottom), pore pressure fluid tubing, three linear variable differential transformers (LVDT) arrayed around the specimen at 120° intervals for the measurement of axial deformations, and an extensometer with a circumferential kit attachment (chain) for the measurement of circumferential deformation. The pressure intensifier assembly provided the confining fluid and pore fluid as well as the confining pressure and pore pressure to the triaxial cell during system operation. Syltherm 800 heat transfer fluid was used as the confining fluid and heating medium. The test equipment also included strain indicators, digital process indicators, temperature profile controller and heating chamber. Strain gauges (active gauges) bonded on the specimen were wired in a half-bridge configuration to the strain indicators connected to the MTS system. During testing, analog signals from the MTS load cell, confining pressure system, strain gauges, LVDTs and circumferential extensometer were scanned at time intervals set by the operator. The signals were converted to engineering units, and the data were stored in the computer. The computer also provided real time plots of stress versus strain throughout the test for the monitoring of the test.

Fig. 3. The completely assembled test stack.

Two types of loading platens were used in these tests: solid platens and platens provided with vents and pore fluid ports for connection to pore pressure fluid tubing. In order to accommodate the strain gauge lead wires,

each bottom platen was fabricated with two diametrically opposed grooves cut parallel to the axis of the platen. Two wires functioning as electrical feedthroughs were embedded in an epoxy-resin (Metaset A4) in each groove as shown in Fig. 4. The inside ends of these two wires were soldered to the strain gauge lead wires before the specimen and the top and bottom platens were encapsulated in a Teflon heat-shrink jacket. After the jacketed stack of specimen and platens had been positioned into the triaxial cell, the outside ends of the wires were connected to the electrical feedthrough connectors located at the bottom of the triaxial cell. The pore pressure fluid tubes were connected to the pore fluid ports in the top and bottom platens, and then to the pore pressure fluid connectors also located at the bottom of the cell. Flow through these tubes was out of the specimen and triaxial cell to an assembly of tubes and valves (Fig. 5), designed for drainage and equipped with transducers for the measurement of pore pressure. For the accurate measurement of pore pressure, trapped air bubbles in the top and bottom platens and pore pressure fluid tubing must be bled out before testing. This was accomplished by running distilled water from the bottom pore fluid tube, through the bottom platen, all the way up the specimen height, through the top platen, down the top pore fluid tube and through the drainage valve to atmosphere.

A reference specimen was required for elevated temperature (non-isothermal) tests. Titanium silicate with a coefficient of thermal expansion of $0.03 \times 10^{-6}/^{\circ}\mathrm{C}$ was used as the reference specimen material. Two pairs of strain gauges (compensation gauges) were applied on the reference specimen (a prism having the dimensions $25 \times 152 \times 6$ mm) and wired to the strain indicators, one for axial strain and one for circumferential strain. When pairs of active strain gauges and compensation gauges were connected as adjacent arms of the half-bridge circuit in the strain indicator, the temperature-induced apparent strains in the active gauges and compensation gauges would cancel exactly, leaving only the stress induced strain in the active gauges to be registered by the strain indicator. The wiring to the strain indicators from the rock specimen and from the reference specimen should be of the same size and length to eliminate the effects of resistance variations in the lead wires. It is also important to use the same types of gauge and glue for the reference specimen as for the rock specimen. Heating of the reference specimen was provided by the heating chamber, which was monitored by a thermocouple wired to the temperature profile controller. The temperature of the reference specimen was synchronized with that of the rock specimen throughout the test.

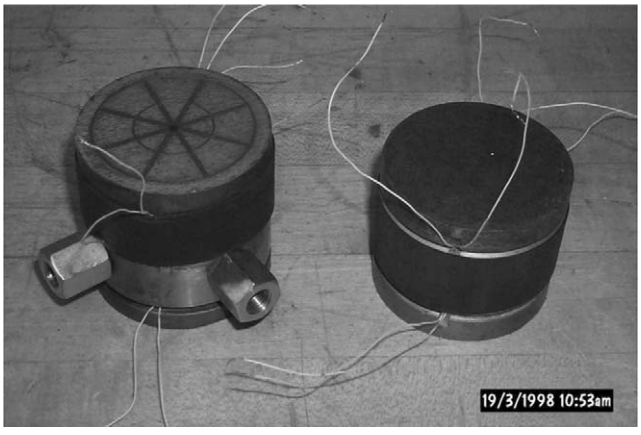

Fig. 4. Special platens used in thermoporoelasticity tests.

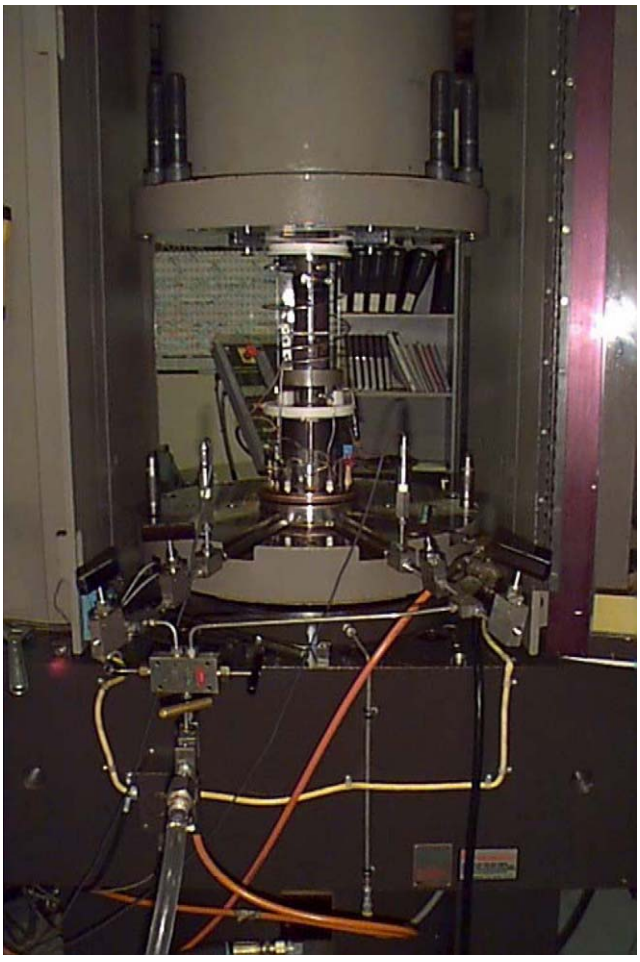

Fig. 5. The assembly of tubes and valves for drainage and pore pressure measurement.

6. Data computation for compression tests

Data obtained from uniaxial and triaxial compression tests included the axial stress, σ_1, confining fluid pressure, σ_3, axial strain, ε_a, and circumferential strain, ε_c. The volumetric strain, ε_v, was computed from ε_a and

ε_c using the following equation:

$$\varepsilon_v = \varepsilon_a + 2\varepsilon_c. \quad (1)$$

The elastic response of the rock was characterized by two elastic parameters: the tangent Young's modulus, E, and the Poisson's ratio, v. The elastic constants were generally determined at the stress level equal to 40% of the peak strength of the specimen. The modulus was derived from the tangent to the σ_1–ε_a curve. A curve fit was first performed on the σ_1 and ε_a data, employing a third order polynomial of the form:

$$\sigma_1 = a_0 + a_1\varepsilon_a + a_2\varepsilon_a^2 + a_3\varepsilon_a^3, \quad (2)$$

where a_0, a_1, a_2 and a_3 are curve-fitting parameters. The tangent Young's modulus as a function of ε_a was defined as the first derivative of Eq. (2), thus representing the slope of the σ_1–ε_a curve.

$$E = a_1 + 2a_2\varepsilon_a + 3a_3\varepsilon_a^2. \quad (3)$$

The axial strain measured when the axial load was at 40% of the peak load was substituted into (3) to calculate a representative value for Young's modulus. An equation for the slope of the σ_1–ε_c curve was derived using a similar approach, and this slope was defined as E_c. Poisson's ratio, v, was equal to E divided by E_c.

7. Damage-controlled tests

The damage-controlled tests were designed to study the evolution of rock damage as a function of the magnitude of the applied stresses. The tests were originally devised from cyclic-loading post-failure tests [27] for the calibration of an elastic-brittle-ductile continuum model [28]. Martin and Chandler [22] later analysed some data from cyclic-loading post-failure tests and found the data useful for investigating the evolution of rock damage within a granite rock specimen.

The damage-controlled tests could be performed under unconfined or confined conditions. Under the confined condition, a confining pressure was first applied to the specimen. Tests were conducted under the axial strain control mode, approximating an axial stress application rate of 0.75 MPa/s. Axial stress was applied in cycles of incremental loading and unloading. The specimen was unloaded when the axial stress attained predefined stress levels, every 40 MPa for example, until the axial stress reached approximately 75% of the estimated peak strength of the rock. Above that stress level, with the specimen rapidly dilating as the rock approached its peak strength, the specimen was unloaded at 0.063-mm increments of circumferential deformation for better control of the test. Each unloading sequence consisted of reducing the axial stress to a value slightly above the confining pressure, except for unconfined tests, which were unloaded to about 5 MPa. Care was taken to prevent violent failure of the specimen, enabling testing to continue into the post-peak region. This was accomplished by programming the MTS system to unload immediately when a drop in the axial load (initial failure) was detected. Loading was then reinitiated until another drop in the axial load or a 0.063-mm increment of circumferential deformation was detected, and the unloading–reloading cycle was repeated. A specimen was repeatedly (cyclically) loaded and unloaded to its peak strength and subsequently taken through post-peak to its residual strength, after which the test was ended. Typical stress and strain data from a damage-controlled test are displayed in Fig. 6.

The values of σ_{cd}, σ_{ci}, E and v were determined for each loading–unloading cycle, and the results were used to study the migration of the loci of σ_{cd}, σ_{ci}, E and v in the pre-peak, peak and post-peak regions. Fig. 7 shows that the σ_{ci}-locus drops slightly with increasing number of cycles. The value of σ_{cd} increases with the number of cycles to a maximum value, defined as the critical crack damage stress σ'_{cd}, in the pre-peak region, and then drops abruptly when the specimen reaches its peak strength, levelling off in the post-peak region. Fig. 7 also shows that the E locus starts to drop at the onset of stable crack growth and then decreases gradually with the increasing number of cycles as damage is accumulated. The v locus can be seen to rise as the E locus falls and levels off at a value above 0.5 in the post-peak region, indicating the departure of the material from elastic behaviour. Damage in Figs. 7 and 8 is defined as the accumulated permanent shear strain measured upon unloading.

With each new incremental loading cycle, new cracks form, old cracks propagate, crack density increases, and the stress required to initiate unstable crack growth becomes lower than that for the previous cycle. This increased damage results in a drop of both σ_{cd}, the value taken to be indicative of the material's long-term

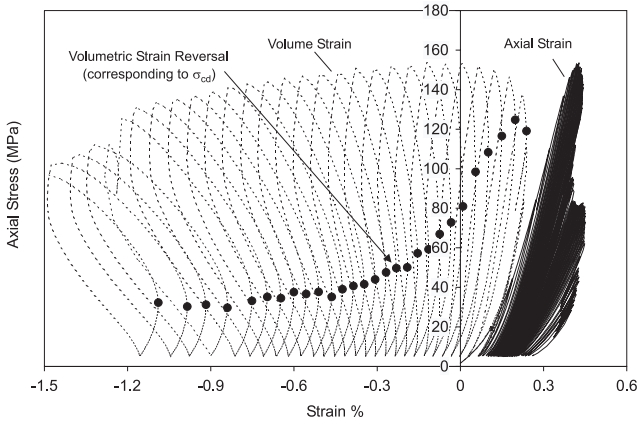

Fig. 6. Plot of axial stress versus axial and volumetric strain for a damage-controlled test.

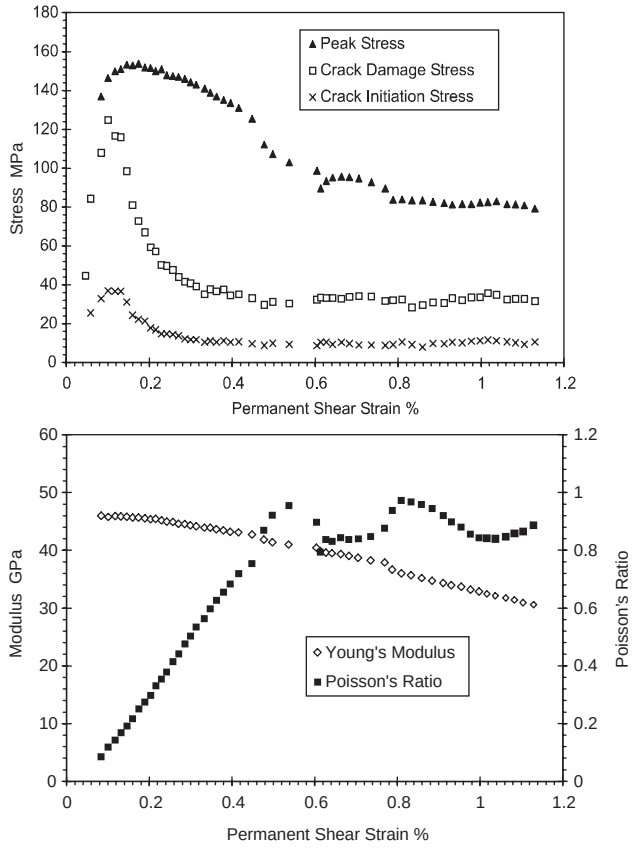

Fig. 7. Plot of peak stress, σ_{cd}, σ_{ci}, E and v versus permanent shear strain for a damage-controlled test.

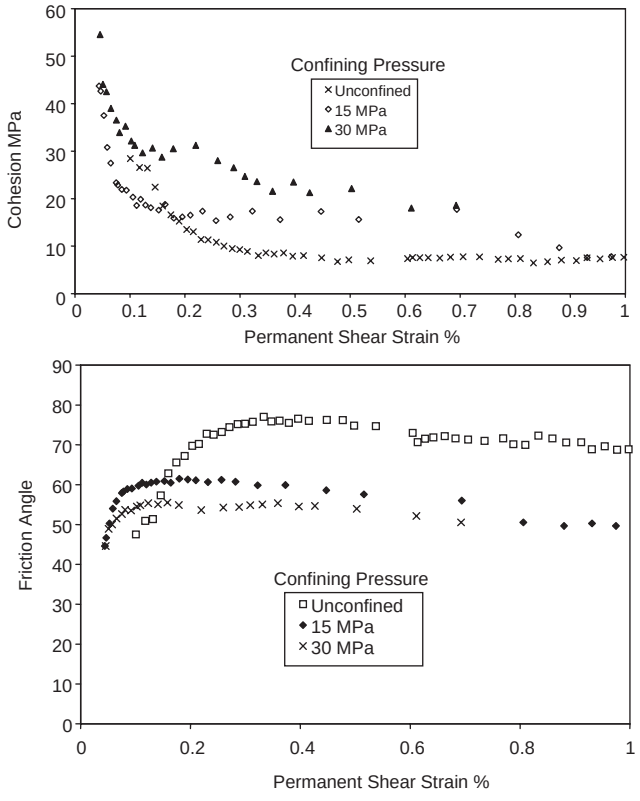

Fig. 8. Decrease in cohesion and mobilization of friction with increasing damage from damage-controlled test data.

strength, and a decrease in elastic modulus E of the damaged rock. A Poisson's ratio above 0.5 is indicative of the volume expansion resulting from the formation and opening of axially aligned microcracks during compressive loading. As the cycles are repeated, the damage is accumulated until the fracturing process is dominated by unstable crack growth and the coalescence of fractures into shear planes. Continued cycling into the post-peak region results in the material degrading to a residual shear strength value. At large strain, Martin [23] found the crack initiation stress, σ_{ci}, to be coincident with the onset of dilation, σ_{cd}.

Martin and Chandler [22] describe the long-term strength, σ_{cd}, in terms of Mohr-Coulomb cohesion and friction. The classical Mohr-Coulomb relation for failure stress, σ_f, for slip along a shear plane is defined as

$$\sigma_f = 2S_0 \tan\left(\frac{\pi}{4}+\frac{\phi}{2}\right) + \sigma_3 \tan^2\left(\frac{\pi}{4}+\frac{\phi}{2}\right), \quad (4)$$

where S_0 is the empirical cohesion intercept, ϕ is the material's theoretical friction angle and σ_3 is the confining stress. The cohesion is the strength of the material just as sliding starts. Friction is mobilized as shear displacement along a shear plane (or microcrack) increases. At the same time as friction is being mobilized, cohesion decreases as the rock becomes more damaged. Martin [23] used stress analyses and in situ acoustic emission data to suggest that the friction angle is zero at the crack initiation stress, σ_{ci}, and that the cohesion is equal to $\frac{1}{2}(\sigma_1-\sigma_3)$ at crack initiation, which for Lac du Bonnet granite is independent of confinement at approximately 35 MPa. Martin also suggested that, under conditions of stable crack propagation, the apparent cohesion, as indicated by the crack damage stress, increases and reaches a maximum, with this maximum value indicative of the long-term rock strength.

The long-term strength of the rock is considered to be σ_{cd} and this strength will have components of cohesion and friction. Substituting σ_{cd} for σ_f in (4) the cohesion, S_0, can be defined as a function of internal friction angle as follows:

$$S_0 = \frac{\sigma_{cd}}{2\tan\left[(\pi/4)+(\phi/2)\right]} - \frac{\sigma_3}{2}\tan\left[\frac{\pi}{4}+\frac{\phi}{2}\right]. \quad (5)$$

Martin and Chandler [22] showed that, for the crack damage threshold (the maximum value of σ_{cd}), $\phi \approx 48^\circ$, which was input into (5) to obtain the initial, or maximum, value of S_0. The mobilized friction angle at

peak stress, σ_f, can then be defined as

$$\phi = \left\{ \begin{array}{ll} 2\tan^{-1}\left[\frac{\sigma_f}{2S_0}\right] - \frac{\pi}{2} & \text{for } \sigma_3 = 0 \\ 2\tan^{-1}\left[\frac{1}{2}\left(\sqrt{\left(\frac{2S_0}{\sigma_3}\right)^2 + 4\frac{\sigma_f}{\sigma_3}} - \frac{2S_0}{\sigma_3}\right)\right] - \frac{\pi}{2} & \text{for } \sigma_3 > 0 \end{array} \right\}. \quad (6)$$

The variations in cohesion and friction angle were calculated using (5) and (6) and measured values of σ_{cd} and σ_f from damage-controlled tests, and plotted as a function of damage (permanent shear strain) in Fig. 8 for samples tested at 0, 15 and 30 MPa confining pressure. Hajiabdolmajid et al. [29] used the mobilization of friction and degradation of cohesion data from these tests, as a function of plastic strain, to model the in situ response of rock to excavation for the Mine-by Experiment tunnel at the URL.

8. Long-term loading tests

Stresses less than, but close to, the peak strength of the rock can only be sustained for a short duration before failure, and the strength as determined from short-term laboratory tests cannot be relied on for the long-term loading the rock experiences in the field. Schmidtke and Lajtai [30] demonstrate this observation to hold true for Lac du Bonnet granite. In theory, if the stress were to be held constant above a certain threshold, the sample would eventually fail, while samples loaded to a constant stress below the threshold could be cracked but remain stable. As noted previously, Martin and Chandler [22] suggested that σ_{cd} was indicative of this threshold for long-term strength. Long-term loading tests were designed to provide a measure of the long-term strength of different rock units (fine and medium grained granite) at different temperatures, to investigate the relationship of σ_{cd} with the long-term strength, to provide stress versus time-to-failure data at different confinement for the calibration of a time-dependent numerical model for rock strength, and to provide an indication of changing materials properties with increasing damage under constant load.

8.1. Time-to-failure under constant load

Long-term loading tests were conducted in four test sequences during a period of four years. Each test sequence was designed to either increase the database of results from the previous sequence, or to obtain additional information by introducing new variations to the testing procedure. In all, over ninety long-term load tests were performed on Lac du Bonnet granite [31–34]. All tests consisted of at least an initial loading stage and a long-term loading or creep stage. Water-saturated specimens were used, and the tests were conducted under drained conditions. In the initial loading stage, after the application of the designed confining pressure, a specimen was loaded to a predetermined creep stress level, σ_{cp}. The tests were performed on both unconfined and confined specimens. In order to compare time-to-failure data at different confinement the creep stress, σ_{cp}, was normalized to a value indicative of the specimen's strength. Since the compressive strength could not be determined, σ_{cd} was used as the reference strength. The ratio of σ_{cp} to σ_{cd} was defined as β, and the applied loads were selected to provide time-to-failure data for a range of β values at different confining stresses.

Two methods were used to establish the σ_{cp} stress level, where σ_{cp} needed to be greater than σ_{cd}, in order to meet target values for β. The first method was to load and unload the specimen in one cycle to determine σ_{cd} and subsequently load the sample to a creep stress equal to the desired value of β multiplied by σ_{cd}. Using this method, the specimen was axially loaded under computer control. The computer was programmed to unload when volumetric strain reversal, σ_{cd}, was detected. The specimen was unloaded to a stress level slightly higher than the confining pressure, and then reloaded until the applied load reached the designed σ_{cp} level. A constant loading–unloading rate of 0.75 MPa/s was used throughout the initial loading stage. It was found that using this two-cycle method, specimens often failed prematurely in the creep stage, since additional damage had accumulated in the rock during the unload-reload cycle before the actual creep test began.

In the second approach, σ_{cd} was first estimated from previous compression tests performed on the same type of rock. The specimen was then loaded directly to the predetermined σ_{cp} level, which was selected to reach a target value of β based on the estimation of σ_{cd}. The actual value of β was then calculated using the value of σ_{cd} determined from data collected during specimen loading. The creep stage started as soon as the applied load reached σ_{cp}, where it was maintained until the specimen failed. However, due to test schedule limitations, if the specimen did not fail after a specific length of time (typically 24 h) of loading, the test was usually discontinued. Data were collected every three seconds during the initial loading stage and every 0.05 to 5 minutes during the creep stage, depending on the length of the test. Only the LVDTs and chain were used for the measurements of ε_a and ε_c in the long-term loading tests.

In some tests, where the specimen did not fail in 24 h, the load was raised to a higher σ_{cp} level, and the creep stage continued. This process could be repeated two or three times until the failure of the specimen occurred. An example of a three-stage loading test is provided in Fig. 9, where the creep stress was raised in its final stage

from 513 to 535 MPa and subsequently failed in 17 h. Although these multi-stage loading tests provided useful observations on rock failure under constant load, it was not possible to use this data in the time-to-failure analysis.

Typical data from a single-stage long-term loading test are provided in Figs. 10 and 11. For granite specimens loaded above the rock's long-term strength, the creep curves (strain versus time) in Fig. 11 were quite similar to those for more ductile materials. The curves exhibited the three classical stages of creep: a very short duration primary, or attenuating, creep followed by an almost linearly increasing transient, or secondary, creep phase and an exponentially increasing tertiary creep phase leading to the failure of the specimen. The observed behaviour indicated a time-dependent deformation associated with crack growth in the rock specimen under constant compressive stress, and the onset of the tertiary creep occurred when the crack density reached a critical value. The lateral, or circumferential, strain indicated a much greater time-dependency than the axial strain, suggesting dilation and opening of vertically aligned cracks under constant load. For those specimens that did not fail, the tertiary creep was absent in the strain–time curves.

The plot of the β, the ratio of σ_{cp} to σ_{cd}, versus time-to-failure reveals the time-dependent failure response as a function of confining stress (Fig. 12). It can be seen that under each confining pressure condition, the time-to-failure increased as β decreased. Also shown in Fig. 12 is the β versus total creep time for those specimens where no failure occurred within the time constraints of the test. For a given value of β, the confining pressure influenced the time-to-failure, with longer times-to-failure at higher confinement. It is reasonable to suggest that at each confining pressure, there exists a static fatigue limit, above which failure of the rock specimen would occur if the test were run long enough. It is impossible to accurately define this limit using loading durations of only a few days or less. In Fig. 13, the stress limit corresponding to no failure after 48 h is compared with σ_{cd} and σ_{ci} for the same tests. If these values are somewhat representative of the static fatigue limit, then σ_{cd} is a reasonable estimate of the

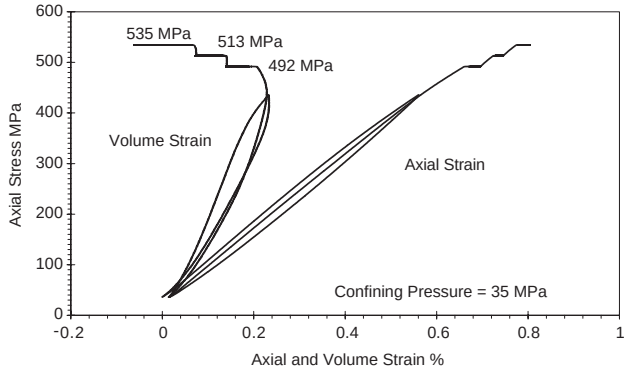

Fig. 9. Axial stress versus axial and volume strain for a three-stage loading test.

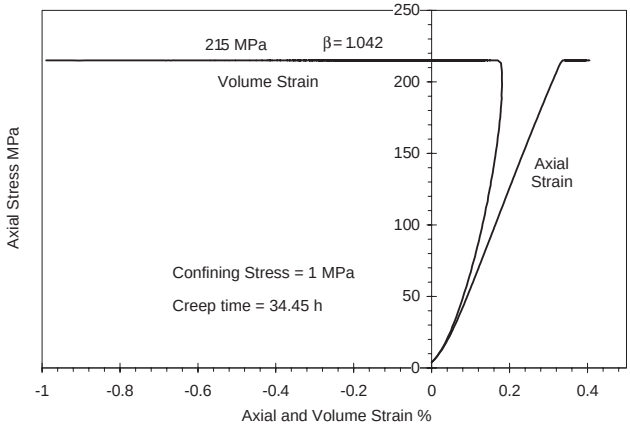

Fig. 10. Axial stress versus strain and volume strain for a long-term load test.

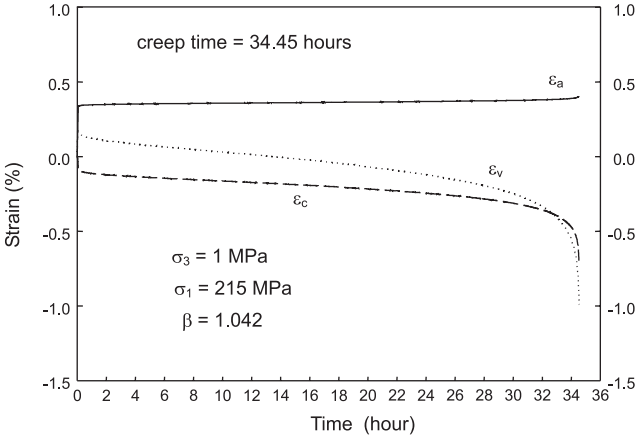

Fig. 11. Axial, circumferential and volume strain versus time for a long-term load test.

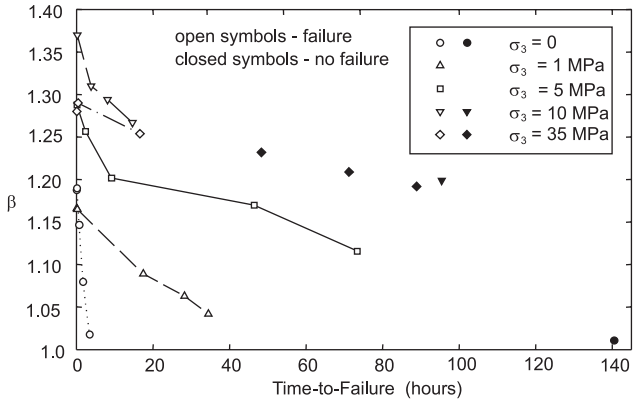

Fig. 12. Plot of β versus time-to-failure for different confining stresses.

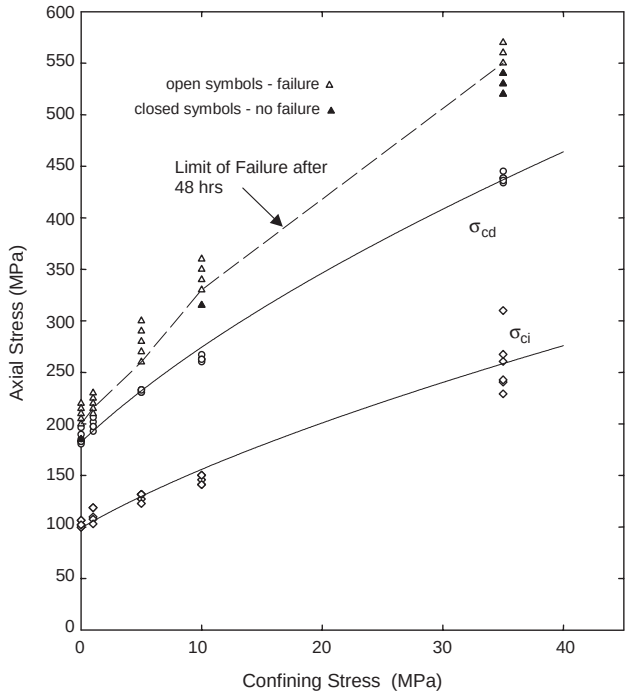

Fig. 13. Comparison of the limit of failure after 48 h with σ_{cd} and σ_{ci} as a function of confining stress.

long-term strength at low confinement, but underestimates the long-term strength at higher confining pressure. For design purposes, however, σ_{cd} would be a conservative estimate of long-term strength at any confining pressure.

The full suite of long-term loading tests included elevated temperature long-term loading tests [33] to study the effect of heating on the time-to-failure response of the rock. Elevated temperature tests were conducted at 50 and 75 °C, and at confining pressures of 0, 1 and 5 MPa. At a given applied stress, marginally shorter time-to-failure was observed when specimens were heated to 75° C. However, heating also resulted in a slightly reduced σ_{cd}, that is, the strength was slightly reduced by heating. Hence β, for a given applied stress, was slightly higher at higher temperatures. The net result of both slightly higher β and shorter times-to-failure was that the relationship between β and time-to-failure was essentially unchanged when the testing temperature was increased from room temperature (23 °C) to 75 °C.

Time-to-failure data from long-term load tests are compared with similar data from Schmidtke and Lajtai [30] on saturated unconfined specimens of Lac du Bonnet granite in Fig. 14. The applied stress is normalized to the peak strength, even though the peak strength could not be measured. Schmidtke and Lajtai estimated the peak strength of each specimen by conducting 14 unconfined strength tests on a parallel set of specimens, matching higher measured strengths to static fatigue specimens with the longest times-to-failure. In order to combine Schmidtke and Lajtai's data with the results

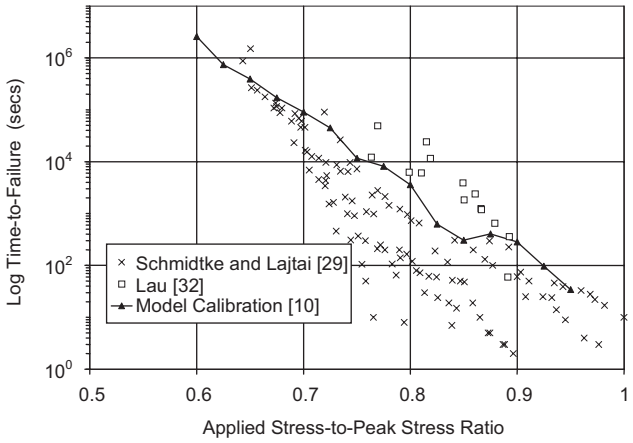

Fig. 14. Comparison of unconfined long-term load test data with static fatigue data from Schmidtke and Lajtai [30] and PFC model calibration results.

from long-term load tests, the value of β for each unconfined test was multiplied by 0.75, which is the average ratio of σ_{cd} to unconfined compressive strength as derived from independent strength tests. The data from Lau [32] appears to have longer-times-to-failure than Schmidtke and Lajtai [30] at a given ratio of applied stress to strength. It is not clear whether this is related to the method for estimating the specimen strength, to test technique or to the location the samples were taken from. Potyondy and Cundall [10] used this combined data set to calibrate their PFC model to the long-term behaviour of Lac du Bonnet granite.

8.2. Elastic properties and damage accumulation

Cyclic long-term loading tests [34] were conducted to investigate the accumulated damage and degradation of elastic properties as a function of the duration of the applied stress. The cyclic long-term loading test was conducted by interrupting the creep stage with a series of unloading–reloading cycles. The specimen was unloaded to a stress level about 5 MPa above the confining pressure and reloaded to the σ_{cp} level again, after which the creep test was resumed. This process was repeated as many times as required to fail the specimen. For each unloading–reloading cycle, σ_{cd}, σ_{ci}, E and v were measured from the reloading curve. The E and v values were determined at the stress level equivalent to 0.5 σ_{cp}. In one test, the specimen was removed from the compression machine after each fully unloading sequence for the measurement of the P-wave (compressional) velocity V_p and S-wave (shear) velocity V_s. These velocity data were used to calculate the dynamic Young's modulus E_u and dynamic Poisson's ratio v_u. Data from this one test are provided in Fig. 15. As damage increased with creep time, decreases in the Young's modulus and crack damage stress and an increase in Poisson's ratio were observed in the test. This

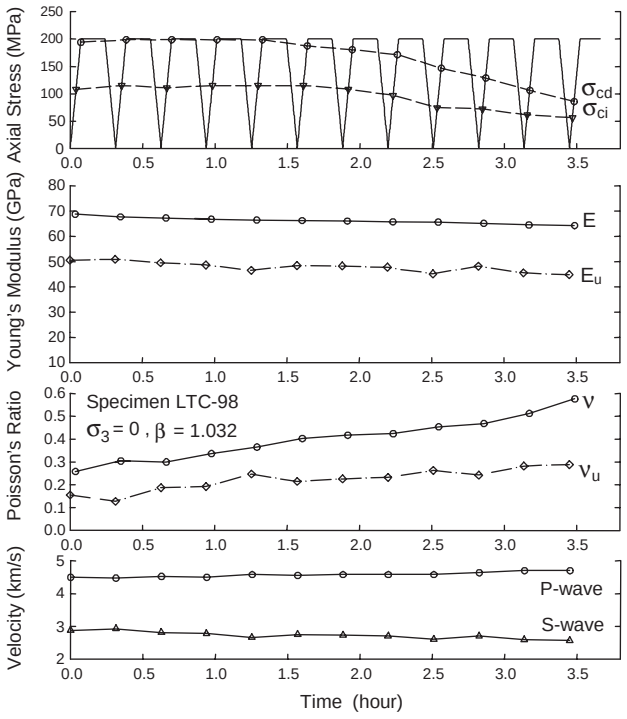

Fig. 15. Plots of axial stress, σ_{cd}, σ_{ci}, Static and dynamic Young's modulus (E and E_u) and Poisson's ratio (v and v_u) and P- and S-wave velocity as a function of time.

result is similar to observations previously noted for the damage-controlled tests (Figs. 6 and 7).

8.3. Combining long-term load tests with damage-controlled tests

The results from the tests were used to define the degradation in strength and elastic properties that would be expected as crack damage increases. For the purpose of this discussion, the damage was quantified in terms of irreversible strain. Strain during the unloading and reloading cycles of the damage-controlled tests included both reversible (elastic) and irreversible components. Strain measured during the constant load portion of the long-term load tests tended to be only inelastic and irreversible. Rock damage is manifested in both the propagation of axially aligned micro-cracks and the shear slip along angled micro-cracks (as shown in the photograph in Fig. 2). Axial crack growth is indicated by increased volumetric strain, whereas, shear slip is indicated by increased shear strain. Measured strain from the damage-controlled tests, the long-term load tests, and from traditional triaxial strength tests were converted to the two octahedral strain parameters: mean strain, which is equal to $\varepsilon_v/3$, and octahedral shear strain, γ_{oct}, which is defined as

$$\gamma_{oct} = \frac{\sqrt{2}}{3}(\varepsilon_a - \varepsilon_c). \quad (7)$$

Plots of octahedral shear strain as a function of mean strain for all three test types are presented in Fig. 16. Data are presented for tests at low (1–2 MPa) and intermediate (10 MPa) confining pressure. The triaxial and damage-controlled test data were calculated up to the maximum axial load, while the long-term load data were provided to the time of sample failure under constant load. The similarities in the plots are remarkable considering the very different stress histories. It is most notable that all the samples from all test types evolve from a linear elastic material, with a positive slope of shear strain versus mean strain, to a cracked and failing sample having a negative slope. The strain path followed for all tests at the same confining pressure is similar regardless of whether the samples were failing under increasing or constant load conditions. The final slope of octahedral shear strain to mean strain was roughly the same for all test types (Fig. 16). This slope indicates that shear strain (slip along angled cracks) and volumetric strain (propagation of axial cracks) were occurring simultaneously and the relative proportion of these strains remained constant in the region of unstable crack growth (greater than σ_{cd} in Fig. 1).

Long-term load tests conducted at various confining pressures are presented in Fig. 17. This plot illustrates a

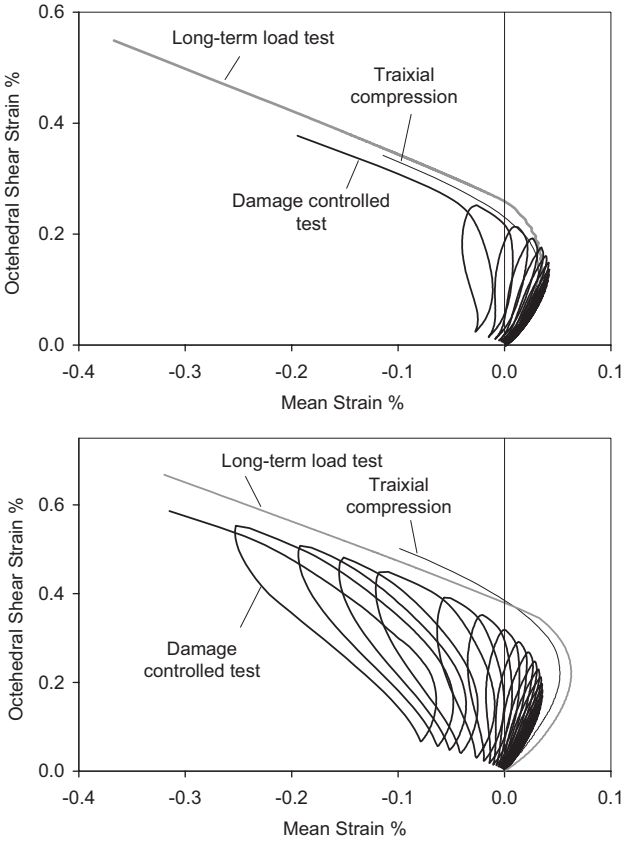

Fig. 16. Octahedral shear strain versus mean strain for triaxial compression, long-term loading and controlled damage tests at 2 MPa (top) and 10 MPa (bottom) confining pressure.

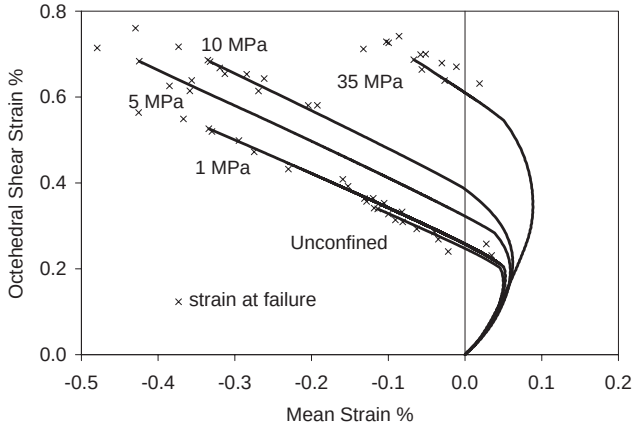

Fig. 17. Octahedral shear strain versus mean strain for long-term loading tests at different confining pressures.

linear relationship between shear strain and mean strain as the sample was loaded towards failure, with the slope being similar for all confining pressures. The slope of mean strain versus octahedral shear strain defines a plastic flow rule for a failing material. This flow rule, in theory, could be used in numerical analyses to define the straining of yielded rock that has exceeded its elastic limit. Also shown in Fig. 17 are the octahedral shear and mean strains at failure for all long-term load tests conducted under the varied applied axial loads. The strain at failure data show that, for confining stresses of 5 MPa or more, most of the long-term load tests failed at octahedral shear strains of between 0.6% and 0.75%. The data suggest a limiting shear strain for tests conducted at higher confining pressures. The tests at higher confinement tended to fail with well developed shear planes, while tests conducted at lower confining stress (2 MPa or less) generally failed by axial splitting at an octahedral shear strain much less than 0.6%. In Fig. 17 these data all plot on a straight line, however, this straight line is coincident with the strain path followed during all low confinement tests and has no value as a failure condition for axial splitting. For the low confinement long-term load tests, samples at lower axial loads had longer times to failure, and generally traveled further along the strain path thus failing at higher shear strain. The strain at failure for samples that split axially, therefore, appeared to be strongly related to the applied stress and did not have an apparent limiting strain.

9. Thermoporoelasticity tests

The objective of the thermoporoelasticity tests was to determine the thermoporoelastic parameters required to model the thermoporoelastic behaviour of rock. The laboratory tests were developed by Detournay and Berchenko [35] and carried out at the MMSL. The thermoporoelasticity tests consisted of five types of tests: drained isothermal test (DIT), undrained isothermal test (UIT), unjacketed isothermal test (UNJ), drained non-isothermal test (DNT) and undrained non-isothermal test (UNT). Tests were performed by applying a confining pressure on the rock specimen. Measurements made in these tests included the changes in confining pressure ΔP, specimen volume, ΔV, and pore pressure, Δp. In the undrained tests, no fluid was allowed to leave the specimen. The non-isothermal tests were conducted by applying a temperature increment θ to the specimen. The unjacketed test was performed by the application of an equal increment $\Delta p'$ to the confining pressure and pore pressure. The boundary conditions, measurements made and parameters determined in the thermoporoelasticity tests are summarized in Table 1. Berchenko [36] proposed that these tests could be carried out in sequence, for example, UIT–DIT–UNT–DNT, and measurements could be made during mechanical and thermal loading as well as unloading.

The thermoporoelasticity tests were developed over a four-year period [2,4] and the results of the tests are provided in a pair of reports [37,38]. Tests were first performed on 145-mm-diameter specimens installed with strain gauges, using a large Hoek triaxial cell, and conducted using the MTS loading system described earlier. Special stainless steel platens, equipped with transducers, pistons, LVDTs and valves, were designed to measure and control pore pressure and pore fluid volume. The reason for using a large specimen was to allow the measurement of the very small volume of fluid expelled from the specimen during a drained test. According to Wissa [39] the ratio of dead fluid volume over the pore fluid volume should be less than 0.003. This ratio, however, was unrealistic for the low porosity granite. In designing the experiment components, the target for allowable dead water space within test system was 20% of the estimated pore volume of the sample. Since the porosity of Lac du Bonnet granite is less than 0.5%, the dead pore water volume, even for the large sample, needed to be on the order of 5 mL. Pore volume and pore pressure were controlled by pistons that could be screwed in or out of very narrow water supply tubes within the loading caps. However, it was found that the large specimen and Hoek cell were difficult to handle, and it was debatable whether the stringent requirements for minimizing dead water space were achieved. Also, the strain gauge lead wires, brought out of the cell via a feed-through hole located at the top of the Hoek cell, were susceptible to damage during loading, affecting the measurement of volume strain. Although the displaced water volume was successfully measured, excessive times were required for pore pressure to equilibrate in the large specimen and there was a lack of consistency between the measured displaced volume between top

Table 1
Summary of thermoporoelasticity tests

Test	Boundary conditions	Measurements	Parameters
DIT	$P = P_0 + \Delta P$ $p = p_0$ $\theta = 0$	$\Delta V/V$	$K = V\Delta P/\Delta V$
UIT	$P = P_0 + \Delta P$ $\zeta = 0$ $\theta = 0$	$\Delta V/V$ Δp	$K_u = V\Delta P/\Delta V$ $B = \Delta p/\Delta P$
UNJ	$P = P_0 + \Delta p'$ $p = p_0 + \Delta p'$ $\theta = 0$	$\Delta V/V$	$1/K_s = \Delta V/V\Delta p'$ $\alpha = 1 - K/K_s$
DNT	$P = P_0$ $p = p_0$ $\theta = T - T_0$	$\Delta V/V$	$\beta_d = \Delta V/V\theta$
UNT	$P = P_0$ $\zeta = 0$ $\theta = T - T_0$	$\Delta V/V$ Δp	$\beta_u = \Delta V/V\theta$ $\alpha/(KB(\beta_m - \alpha\beta)) = \theta/\Delta p$

Note: T = temperature and the subscript "0" denotes the initial value.

and bottom platens. Under these circumstances, the thermoporoelasticity tests underwent major modifications. The measurement of fluid volume change was eliminated, thus allowing the specimen size to be reduced from 145-mm-diameter to 61-mm-diameter, permitting the tests to be conducted in a regular triaxial cell using the MTS loading system. This change in equipment allowed improved test temperature control, improved methods for pore pressure monitoring and the use of proven methods for strain gauge lead wire routing.

The breakdown of the strain gauge bonding during testing was a persistent problem in the thermoporoelasticity tests. Innovative procedures for the installation of strain gauges on wet specimens were introduced. The procedures involved three applications of adhesives and coating. The gauging area was first dried and glue was applied to fill surface irregularities and seal pores. A cure time of at least 6 h was allowed for the glue to set. The gauging area was then abraded to remove extra glue on the rock surface, and the strain gauge was installed, using the same glue. Again, a cure time of at least 6 h was required. After lead attachment, a thick coat was applied on and completely covered the gauge and solder joints for moisture protection. During the curing of the glue and coating, the rest of the specimen was covered by wet paper to reduce the loss of moisture from the specimen. Micro-Measurements M-Bond AE-10, M-Bond 200, M-Coat and Lord 410/#17 acrylic adhesive were used as the glue at different stages of the testing program. The Lord 410/#17 acrylic adhesive was found to perform most satisfactorily on the wet specimens. However, the Lord 410/#17 adhesive has an operating range of only 20–38 °C.

Data obtained from these tests included the axial stress, σ_1, confining stress, σ_3, axial and circumferential strain, ε_a and ε_c, pore pressure, p, and temperature, T. The volumetric strain, ε_v, was computed using (1). It should be noted that only strain gauges were used for the measurements of ε_a and ε_c because the LVDTs and chain were not calibrated for thermal expansion and the chain did not appear to be able to measure contraction during cooling.

9.1. Drained isothermal test

In the DIT, the mean stress, P, was raised in increments of 1 or 2 MPa, while the temperature remained constant. The mean stress was defined as

$$P = \frac{1}{3}(\sigma_1 + 2\sigma_3). \tag{8}$$

Water was permitted to leave the specimen and the induced pore pressure dissipated by opening all the drainage valves at the bottom of the triaxial cell. Detournay and Berchenko [35] suggested that the time, t, for the dissipation of the stress-induced pore pressure is of the order of $L^2/4c$, where c is the diffusivity coefficient and L is the length of the specimen. For the granite, $c = 2 \times 10^{-6}\,m^2/s$ and t was estimated to be 50 min for a 154-mm-long specimen. At least one hour was therefore allowed between increments of P. The pore pressure within the specimen had to be in equilibrium with the applied pore pressure before the ε_v measurement became meaningful. A plot of P versus ε_v for the determination of the drained bulk modulus K is illustrated in Fig. 18.

9.2. Undrained isothermal test

The UIT was similar to the DIT, except that no fluid was permitted to leave the specimen. Accurate

determination of B required that the dead water volume be kept to a minimum in the undrained tests, as the existence of this volume permitted fluid to escape the specimen [35]. In the UIT, a waiting period of at least ten minutes was allowed between increments of P, so that a minimum of three readings of ε_a and ε_c could be taken. Pore pressure was measured at the top and bottom ends of the specimen immediately after each increment of P. Fig. 19 reveals that p increases steadily with P, and the slope of the p versus P curve represents the value of Skempton coefficient, B. P was also plotted against ε_v (Fig. 20) to obtain the undrained bulk modulus K_u using the relationship in Table 1.

9.3. Drained non-isothermal test

The DNT was carried out by raising the temperature of the rock specimen and the reference specimen simultaneously in steps, while P remained constant. The rock was heated at a rate of less than 1 °C per minute until the test temperature was reached. The low heating rate was necessary to eliminate cracking due to the stress produced by thermal gradients in the rock specimen [40]. In each step, a thermal equalization period of one hour was also required to ensure that the specimen was uniformly heated throughout. It was difficult to estimate the time for the dissipation of the temperature-induced pore pressure due to the coupling between mechanical and thermal fields. The pore pressure field had to be in equilibrium with the boundary condition before the ε_v measurements became meaningful. A draining period of at least 4 h was allowed between increments of temperature. Fig. 21 shows the plots of temperature and ε_v versus time. In this test, the specimen was permitted to drain overnight after the first increment of T. The decrease (expansion) in ε_v due to each temperature increment was recorded, and the drained thermal expansivity, β_d, was calculated. The value of β_d is the volumetric thermal expansivity and, in theory, is equal to three times the linear coefficient of thermal expansivity. Note that data recorded during heating, soaking and drainage were excluded from analysis.

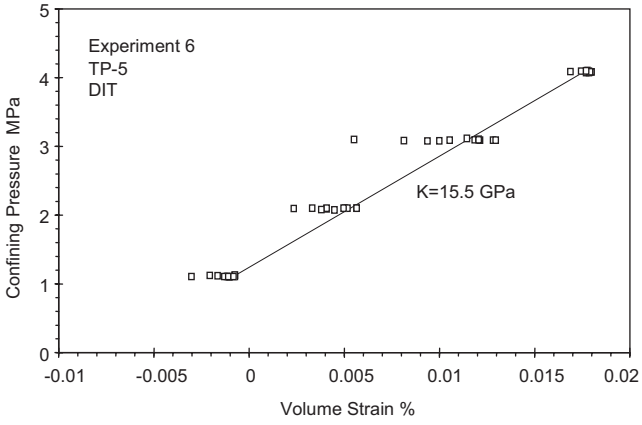

Fig. 18. Plot of confining stress versus volumetric strain for the DIT.

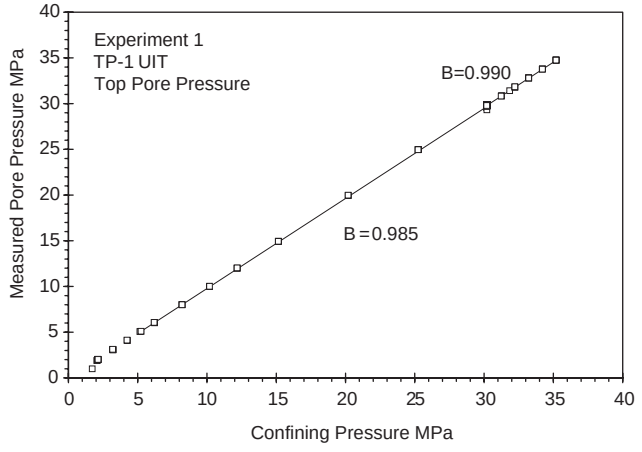

Fig. 19. Plot of pore pressure versus confining pressure for the UIT.

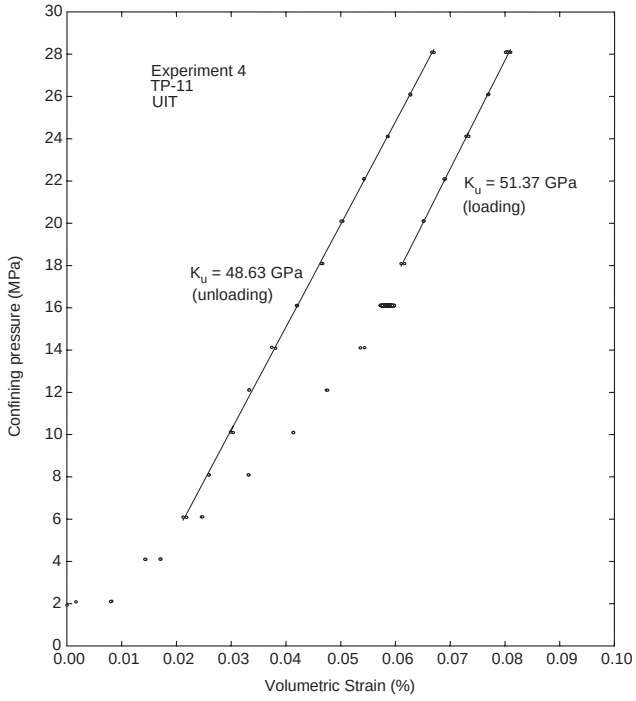

Fig. 20. Plot of confining pressure versus volumetric strain for the UIT.

9.4. Undrained non-isothermal test

The UNT was similar to the DNT, except that no fluid was permitted to leave the specimen. The plots of T and ε_v versus time for the determination of the undrained thermal expansivity, β_u are shown in Fig. 22.

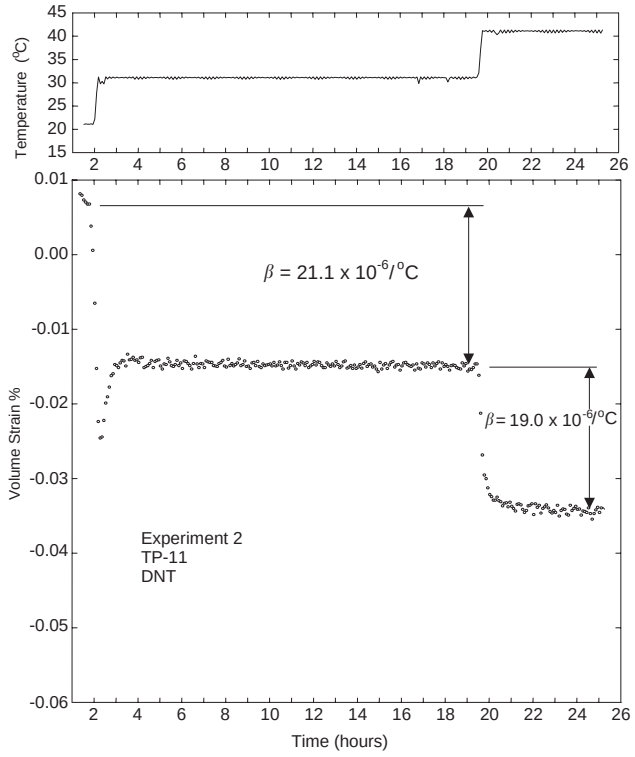

Fig. 21. Plot of temperature and volumetric strain versus time for the DNT.

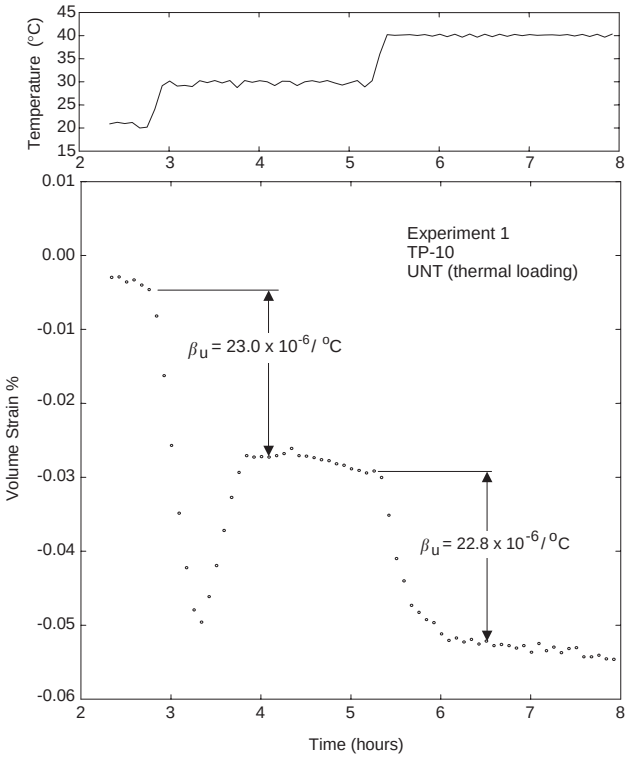

Fig. 22. Plot of temperature and volumetric strain versus time for the UNT.

It is worth noting that the trough in the ε_v-time plot is probably due to erroneous ε_v measurements caused by some temperature differences between the active and compensation strain gauges. A difference of 1 °C in the temperature between the active and compensation gauges could introduce an error of 15×10^{-6} to ε_a and ε_c, resulting in an error of 45×10^{-6} to ε_v. Considering the very small thermal expansivity of the granite, the error was very large. In future tests, it is suggested to place the reference specimen inside the triaxial cell to ensure both the rock specimen and reference specimen have the same temperature, but extra electrical feedthrough connectors for the triaxial cell would be required.

As in the UIT, a one hour thermal equalization period was allowed, and only ε_v data recorded after the soak time were used to calculate β_u. The plots of pore pressure versus temperature for the UNT are displayed in Fig. 23. The pore pressure can be seen to increase with each raise in temperature and then start to drop slowly. It was difficult to decide which data pairs (p, T) should be used for the determination of the lumped parameter function $\Delta p/\theta$. For this test, only the six data pairs recorded just before the temperature was raised and the data pairs with the six highest p values recorded after the temperature had been raised were used. A linear regression was performed on the data pairs and $\Delta p/\theta$ was derived from the slope of the regression line. It

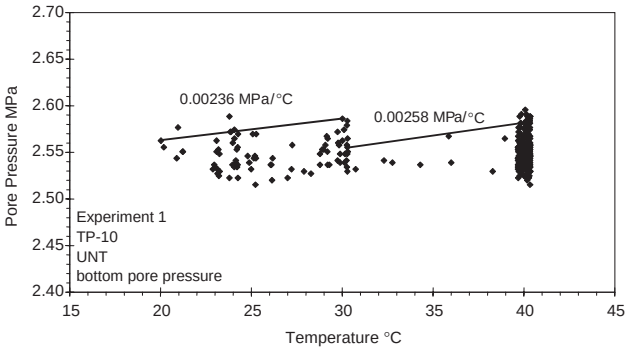

Fig. 23. Plot of pore pressure versus temperature for the UNT.

should be noted that the $\Delta p/\theta$ values computed in the test are not representative of in situ conditions, as the laboratory samples are not volumetrically constrained as they would be in the field. The value of $\Delta p/\theta$ measured in the UNT was used to calculate the hydrothermal coupling coefficient β_m (defined in Table 1).

9.5. Unjacketed isothermal test

The UNJ was performed without any jacket on the specimen. The method was similar to the original unjacketed test proposed by Biot and Willis [41]. The

UNJ was conducted by imposing equal increment $\Delta p'$ to the confining pressure and pore pressure. A waiting period of at least ten minutes was allowed so that a minimum of three readings could be taken. Fig. 24 displays the P–ε_v plot for the UNJ. The slope of the P–ε_v curve represents the bulk modulus of the solid mineral constituents of the rock K_s, and the Biot coefficient, α, could be computed from the values of K and K_s (as defined in Table 1).

9.6. Discussion

Over 40 thermoporoelasticity tests were performed in the test program. The mean values of the thermoporoelastic parameters are compared with the pre-test estimated values provided by Detournay and Berchenko [35] in Table 2. The biggest difference between the tests performed in 1998 and 1999 was an improved method for performing the unjacketed test, allowing a better estimate of K_s and α and the subsequent calculation of β_m. Another improvement was an improved method for applying strain gauges to the specimens resulting in a better bond for testing. The measured strains were used to determine volume change and, hence, to calculate bulk modulus and thermal expansivity.

It can be seen that the modulus values (K, K_u and K_s) obtained in this testing program are slightly lower than the estimated values. The α value agrees very well with the estimated value, while the B and $\Delta p/\theta$ values are lower than the estimated values. It should be noted that the transducers for the measurement of pore pressure in these tests were installed outside the triaxial cell and connected to the loading platen through pore pressure tubes. The accuracy of the pore pressure measurement and the resulting B and $\Delta p/\theta$ values can be improved by locating the transducers closer to the specimen at the loading platens. Although the β_d, β_u and β_m are considerably higher than the estimated values, the fact that similar values of β_d and β_u were obtained in different temperature increments offers reasonable confidence in the accuracy of the results.

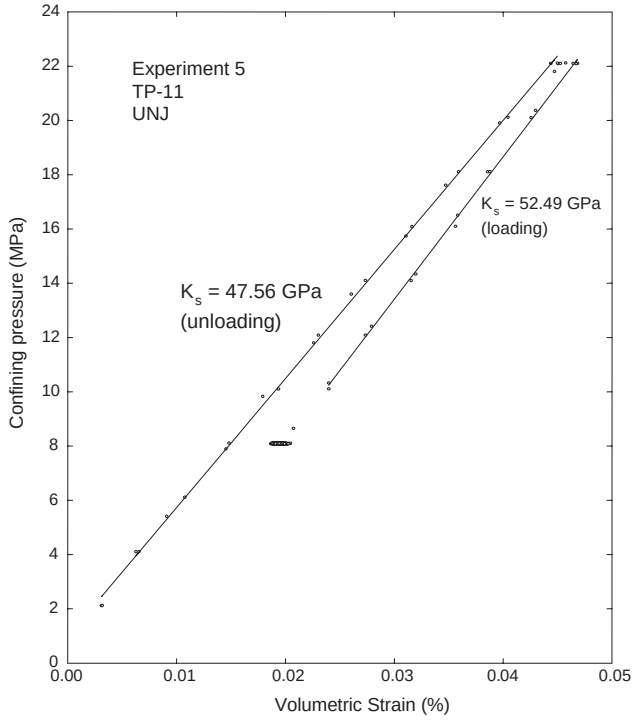

Fig. 24. Plot of confining pressure versus volumetric strain for the UNJ.

The consistence of the measurements of thermoporoelasticity parameters can be tested [35] by substituting the measured values of K, K_u, β_d, β_u and B into (9) to determine β_m:

$$\beta_m = \frac{1}{B}\left(\beta_u - \frac{K}{K_u}\beta_d\right). \tag{9}$$

The computed β_u value of $20.6\times10^{-6}/^{\circ}\mathrm{C}$ compares reasonably well with the value of $23.7\times10^{-6}/^{\circ}\mathrm{C}$ determined from the UNT. The consistency of all isothermal tests can also be checked by calculating K using the measured values of K_u, α and B and the following relation:

$$K = K_u(1-\alpha B). \tag{10}$$

The K value of 14.33 GPa computed using (10) compares fairly well with the measured value of 13.36 GPa. The values determined in the laboratory can also be compared with a field-measured parameter. Senjuntichai and Detournay [42] derived a lumped thermo-hydro coupling parameter, γ, from field tests at the URL [13]. γ is related to the parameters measured in the thermoporoelastic laboratory tests using

$$\gamma = \frac{\beta_0}{S}, \tag{11}$$

where

$$\beta_0 = \beta_m - \frac{3\alpha\beta_d K}{3K+4G},\quad S = \frac{\phi}{K_f} + \frac{\alpha-\phi}{K_s} + \frac{3\alpha^2}{3K+4G}$$

$$\text{and } G = \frac{3}{2}K\frac{1-2v}{1+v}$$

with ϕ being the porosity, G the shear modulus, and K_f the bulk modulus of water. Using the laboratory measured values in Table 2, a porosity of 0.2%, a Poisson's ratio of 0.1, and a fluid bulk modulus of 2.2 GPa, the calculated value of γ , using (11), is 300 kPa/°C. Although this does not correspond exactly with the field measured γ of 430 kPa/°C [42] it is reasonable considering the uncertainty of many of the measured parameters involved, and the potential for differences between properties determined in situ and those determined in the laboratory.

Table 2
Estimated and measured values of thermoporoelastic parameters

Parameter	Estimated value	1998 measured value	1999 measured value
B	0.98	0.977 ± 0.018	0.908 ± 0.069
K_u (GPa)	52	47.10 ± 4.51	49.97 ± 1.37
K (GPa)	15	13.64 ± 4.46	13.36
$\beta_u (\times 10^{-6}/^\circ C)$	9.9–14.5	26.4 ± 18.9	23.7 ± 1.2
$\beta_d (\times 10^{-6}/^\circ C)$	9	30.8 ± 6.8	20.1 ± 1.5
$\Delta p/\theta$ (MPa/°C)	0.02–0.09	0.017 ± 0.008	0.00419 ± 0.00166
K_s(GPa)	55		50.03 ± 3.49
α	0.73		0.73
$\beta_m (\times 10^{-6}/^\circ C)$	7.5–12.0		15.6

10. Summary

Three laboratory test techniques were developed to provide a measure of in situ long-term rock strength, to quantify the evolution of rock damage as a function of the magnitude and duration of the applied stresses, and to provide data for use in the calibration and solution of numerical models. These techniques were damage-controlled tests, long-term loading tests and thermoporoelasticity tests. Tests were performed on cylindrical rock specimens in a computer-controlled, servo-hydraulic compression machine, equipped with a triaxial cell, heater and instruments for the measurements of deformations, pore pressure and temperature.

The damage-controlled tests were performed with incremental loading–unloading cycles. The determination of the changes in σ_{cd}, σ_{ci}, E and ν with each successive cycle permitted the study of the evolution of damage as a function of the magnitude of the applied stresses. The decreases of σ_{cd}, σ_{ci} and E and the increase of ν with the increasing number of cycles indicated the accumulation of damage. Damage was quantified by measuring the irreversible shear strain upon unloading and the degradation of rock strength and elastic properties.

In the long-term loading tests, an axial stress greater than σ_{cd} was applied to the rock specimen and held constant until failure. The tests demonstrated that σ_{cd} is a reasonable estimate of the long-term rock strength, particularly at low confinement. The time-to-failure was dependent upon the creep stress-to-crack damage stress ratio β and confining pressure. The time-to-failure was found to increase with decreasing β and increasing confining pressure. Damage as a function of the duration of the applied stress was quantified by determining the degradation of elastic properties through periodic unloading–reloading cycles in some tests. As damage increased, the Young's modulus was shown to decrease and Poisson's ratio increase. The test data were found to be useful for the calibration of a time-dependent PFC model for the Lac du Bonnet granite.

Thermoporoelasticity tests were designed to determine the thermoporoelastic parameters required for the modelling of the thermoporoelastic response of rock. The thermoporoelasticity tests consisted of the drained isothermal test (DIT), undrained isothermal test (UIT), unjacketed isothermal test (UNJ), drained non-isothermal test (DNT) and undrained non-isothermal test (UNT). Tests were performed by applying increments of confining pressure, temperature or pore pressure on the rock specimens. Measurements made in the tests included changes in confining pressure, specimen volume and pore pressure. The parameters K, K_u, α, B, β_d, β_u and β_m were determined for the Lac du Bonnet granite by conducting these tests. The consistency of the parameters was checked and their values were compared with estimated values. With the exception of β_d and β_u, the measured values agree reasonably well with the estimated values. Although the β_d and β_u values are considerably higher than the estimated values, the fact that the results could be repeated offers some confidence to the accuracy of the results.

Acknowledgements

The work described in this paper was first funded jointly by Atomic Energy of Canada Limited and Ontario Power Generation (OPG, formerly Ontario Hydro) under the auspices of the CANDU Owners Group and later by OPG for application in their Deep Geologic Repository Technology Program. The authors wish to acknowledge the support of the staff of the Mining and Mineral Sciences Laboratories (formerly Mining Research Laboratories), particularly Bernie Gorski, Blain Conlon and Ted Anderson.

References

[1] Read RS, Chandler NA. Excavation damage and stability studies at the URL—rock mechanics considerations for nuclear fuel waste disposal in Canada. In: Proceedings of the 37th US Rock Mechanics Symposium, Vail, Colorado, 1999. p. 861–8.

[2] Martino JB, Chandler NA. Summary report on thermal hydraulic studies in granite 1994 to 1999. Ontario Hydro Nuclear Waste Management Division Report 06819-REP-01200-00092-R00, 1999*.

[3] Chandler N, Read R, Cundall P, Potyondy D, Detournay E, Young RP, Lau JSO. An integrated approach to excavation design—A project within Canada's used fuel disposal program. In Pacific Rocks 2000, Proceedings of the Fourth North American Rock Mechanics Symposium, Seattle, Washington, 2000. p. 1271–8.

[4] Read RS, Chandler NA. An approach to excavation design for a nuclear fuel waste repository—the thermal-mechanical stability study final report. Ontario Power Generation Nuclear Waste Management Division Report 06819-REP-01200-10086-R00, 2002*.

[5] Detournay E, Berchenko I, Chandler N. Thermoporoelastic analysis of the URL Buffer/Container Experiment. In: Amadei Kranz Scott Smeallie, editor. Proceedings 1996 International Conference on Deep Geological Disposal of Radioactive Waste, Winnipeg, Manitoba, 1996. p. 6-23–6-30.

[6] Chandler NA, Read RS, Wan AWL. Implications of the results of URL experiments on the design of repository seals in granite. In: Proceedings 1996 International Conference on Deep Geological Disposal of Radioactive Waste, Winnipeg, Manitoba, 1996. p. 7-1–7-10.

[7] Read RS, Martino JB. Effect of thermal stresses on progressive rock failure at AECL's Underground Research Laboratory. In: Proceedings 1996 International Conference on Deep Geological Disposal of Radioactive Waste, Winnipeg, Manitoba, 1996. p. 7-43–7-53.

[8] Martin CD, Read RS. Strength of massive granite around underground excavations. In: Proceedings of the 16th Canadian Rock Mechanics Symposium, Sudbury, Ontario, 1992. p. 1–11.

[9] Itasca Consulting Group Inc., PFC2D particle flow code in 2 dimensions, Verson 2.0. Minneapolis, Minnesota, USA, 1999.

[10] Potyondy DO, Cundall PA. A bonded-particle model for crystalline rock. Int J Rock Mech Min Sci 2004;41(8).

[11] Potyondy DO, Cundall PA. Modeling notch-formation mechanisms in the URL Mine-by Test Tunnel using bonded assemblies of circular particles. Int J Rock Mech Min Sci 1998;35:510–1.

[12] Potyondy DO, Cundall PA. The PFC model for rock: predicting rock mass damage at the underground research laboratory. Ontario Power Generation Nuclear Waste Management Division Report 06819-REP-01200-10061-R00, 2001*.

[13] Berchenko I, Detournay E, Chandler NA, Martino JB, Kozak ET. An in-situ thermo-hydraulic experiment in a saturated granite. Part I: Design and results. Int J Rock Mech Min Sci 2004;41(8).

[14] Lau JSO, Gorski B, Jackson R. Some rock mechanics laboratory testing related to the construction and operation of AECL's underground research laboratory (URL). In Proceedings 1996 International Conference on Deep Geological Disposal of Radioactive Waste, Winnipeg, Manitoba, 1996. p. 7-31–7-41.

[15] Lau JSO. Rock mechanics laboratory testing for nuclear fuel waste disposal vault design. Ontario Power Generation Nuclear Waste Management Division Report 06819-REP-01200-0084-R00, 1999*.

[16] Chandler N, Lau JSO. In situ granite strength examined using non-traditional laboratory techniques. In: Hammah Bawden, Curran Telesnicki, editors. Proceedings of the Fifth North American Rock Mechanics Symposium and the 17th Tunnelling Association of Canada Conference, Toronto, Ontario, 2002. pp. 489–96.

[17] Brace WF, Paulding BW, Scholz C. Dilatancy in the fracture of crystalline rocks. J Geophys Res 1966;71:3939–53.

[18] Bieniawski ZT. Mechanism of brittle fracture of rock, Parts I, II and III. Int J Rock Mech Min Sci Geomech Abstr 1967;4:395–430.

[19] Wawersik WR, Fairhurst C. A study of brittle rock fracture in laboratory compression experiments. Int J Rock Mech Min Sci Geomech Abstr 1970;7:561–75.

[20] Hallbauer DK, Wagner H, Cook NGW. Some observations concerning the microscopic and mechanical behaviour of quartzite specimens in stiff, triaxial compression tests. Int J Rock Mech Min Sci Geomech Abstr 1973;10:713–26.

[21] Kemeny JM, Cook NGW. Micromechanics of deformation in rocks. In: Shah editor. Toughening mechanisms in quasi-brittle materials. Dordrecht: Kluwer Academic Publishers; 1991. p. 155–88.

[22] Martin CD, Chandler NA. The progressive fracture of Lac du Bonnet granite. Int J Rock Mech Min Sci Geomech Abstr 1994;31:643–59.

[23] Martin CD. The strength of massive Lac du Bonnet granite around underground openings. Ph.D. Thesis, University of Manitoba, Winnipeg. 1993.

[24] Mitaim S, Detournay E. Damage around a cylindrical underground opening in hard rock. Int J Rock Mech Min Sci 2004;41(8).

[25] Selvadurai APS, Nguyen TS. Scoping analysis of the coupled thermal-hydrological-mechanical behaviour of the rock mass around a nuclear waste repository. In: Proceedings Workshop on Hydro-thermo-mechanics of Engineered Clay Barriers and Geological Barriers. McGill University, Montreal, 1995.

[26] Detournay E, Senjuntichai T, Berchenko I, Lecampion B. An in-situ thermo-hydraulic experiment in a saturated granite. Part II: Analysis and parameter estimation. Int J Rock Mech Min Sci 2004;41(8).

[27] Lau JSO, Gorski B. The post-failure behaviour of the Lac du Bonnet grey granite. CANMET report MRL 91-079(TR), Energy, Mines and Resources Canada, 1991.

[28] Ofoegbu GI, Curran JH. Deformability of intact rock. Int J Rock Mech Min Sci Geomech Abstr 1992;29:35–48.

[29] Hajiabdolmajid V, Martin CD, Kaiser PK. Modelling brittle failure of rock. Int J Rock Mech Min Sci 2002;39:731–41.

[30] Schmidtke RH, Lajtai E. The long-term strength of Lac du Bonnet granite. Int J Rock Mech Min Sci Geomech Abstr 1985;22:461–5.

[31] Lau JSO, Gorski B, Conlon B. Long-term loading tests on saturated Lac du Bonnet pink granite. Ontario Hydro Nuclear Waste Management Division Report 06819-REP-01200-10003-R00, 1999*.

[32] Lau JSO, Gorski B, Conlon B, Anderson T. Long-term loading tests on saturated granite and granodiorite. Ontario Power Generation Nuclear Waste Management Division Report 06819-REP-01300-10016-R00, 2000*.

[33] Lau JSO. Elevated temperature long-term loading tests on Lac du Bonnet pink granite. Ontario Power Generation Nuclear Waste Management Division Report 06819-REP-01300-10017-R00, 2001*.

[34] Lau JSO. Cyclic long-term loading tests on Lac du Bonnet pink granite. Ontario Power Generation Nuclear Waste Management Division Report 06819-REP-01300-10018-R00, 2001*.

[35] Detournay E, Berchenko, I. Thermoporoelastic response in low porosity rock: characterization of material properties and numerical modeling of near-field rock pore pressures. Ontario Power Generation Nuclear Waste Management Division Report 06819-REP-01200-10067-R00, 2001*.

*Available from Ontario Power Generation Inc., Nuclear Waste Management Division (16th Floor), 700 University Avenue, Toronto, Ontario, M5G 1X6.

[36] Berchenko I. Thermal loading of a saturated rock mass: field experiment and modeling using thermoporoelastic singular solutions. Ph.D. Thesis. Department of Civil Engineering, University of Minnesota, 1998.

[37] Lau JSO, Gorski B, Conlon B, Anderson T. Determination of thermoporoelastic properties of granite using a triaxial cell. Attachment 1 to Summary report on thermal-hydraulic studies 1994 to 1999. Ontario Hydro Nuclear Waste Management Division Report No 06819-REP-01200-0092-R00, 1999*.

[38] Lau JSO, Gorski B, Conlon B, Anderson T. The measurement of thermoporoelastic parameters of granite using a triaxial cell. Attachment to The incorporation of rock pore pressure in repository design and excavation stability analysis. Ontario Power Generation Nuclear Waste Management Division Report 068190REP-10068-R00, 2001*.

[39] Wissa AEZ. Pore pressure measurement in saturated stiff soils. ASCE J Soil Mech Found Div 1969;95(SM4):1063–73.

[40] Richter D, Simmons G. Thermal expansion behaviour of igneous rocks. Int J Rock Mech Min Sci 1974;11:403–11.

[41] Biot MA, Willis DG. The elastic coefficients of the theory of consolidation. J Appl Mech 1957;24:594–601.

[42] Senjuntichai T, Detournay E. Back analysis of field thermo-hydraulic experiments at URL. Attachment 2 to Summary report on thermal-hydraulic studies 1994 to 1999. Ontario Hydro Nuclear Waste Management Division Report No. 06819-REP-01200-0092-R0, 1999*.